



Directly Tracing Cool Filamentary Accretion over >100 kpc into the Interstellar Medium of a Quasar Host at $z = 1$

Sean D. Johnson¹ , Joop Schaye² , Gregory L. Walth³ , Jennifer I-Hsiu Li¹ , Gwen C. Rudie⁴ , Hsiao-Wen Chen⁵ , Mandy C. Chen⁵ , Benoît Epinat^{6,7}, Massimo Gaspari⁸ , Sebastiano Cantalupo⁹ , Wolfram Kollatschny¹⁰ , Zhuoqi (Will) Liu¹ , and Sowgat Muzahid¹¹

¹ Department of Astronomy, University of Michigan, 1085 S. University, Ann Arbor, MI 48109, USA; seanjoh@umich.edu

² Leiden Observatory, Leiden University, PO Box 9513, NL-2300 RA Leiden, The Netherlands

³ IPAC, California Institute of Technology, Mail Code 314-6, 1200 E. California Boulevard, Pasadena, CA 91125, USA

⁴ The Observatories of the Carnegie Institution for Science, 813 Santa Barbara Street, Pasadena, CA 91101, USA

⁵ Department of Astronomy & Astrophysics, The University of Chicago, Chicago, IL 60637, USA

⁶ Aix Marseille Univ, CNRS, CNES, LAM, Marseille, France

⁷ Canada-France-Hawaii Telescope, CNRS, Kamuela, HI 96743, USA

⁸ Department of Astrophysical Sciences, Princeton University, 4 Ivy Lane, Princeton, NJ 08544-1001, USA

⁹ Department of Physics, University of Milan Bicocca, Piazza della Scienza 3, I-20126 Milano, Italy

¹⁰ Institut für Astrophysik, Universität Göttingen, Friedrich-Hund Platz 1, D-37077 Göttingen, Germany

¹¹ Inter-University Centre for Astronomy and Astrophysics (IUCAA), Post Bag 4, Ganeshkhind, Pune 411 007, India

Received 2022 September 9; revised 2022 November 8; accepted 2022 November 10; published 2022 November 29

Abstract

We report the discovery of giant (50–100 kpc) [O II] emitting nebulae with MUSE in the field of TXS 0206–048, a luminous quasar at $z = 1.13$. “Down-the-barrel” UV spectra of the quasar show absorption at velocities coincident with those of the extended nebulae, enabling new insights into inflows and outflows around the quasar host. One nebula exhibits a filamentary morphology extending over 120 kpc from the halo toward the quasar and intersecting with another nebula surrounding the quasar host with a radius of 50 kpc. This is the longest cool filament observed to date and arises at higher redshift and in a less massive system than those in cool-core clusters. The filamentary nebula has line-of-sight velocities >300 km s⁻¹ from nearby galaxies but matches that of the nebula surrounding the quasar host where they intersect, consistent with accretion of cool intergalactic or circumgalactic medium or cooling hot halo gas. The kinematics of the nebulae surrounding the quasar host are unusual and complex, with redshifted and blueshifted spiral-like structures. The emission velocities at 5–10 kpc from the quasar match those of inflowing absorbing gas observed in UV spectra of the quasar. Together, the extended nebulae and associated redshifted absorption represent a compelling case of cool, filamentary gas accretion from halo scales into the extended interstellar medium and toward the nucleus of a massive quasar host. The inflow rate implied by the combined emission and absorption constraints is well below levels required to sustain the quasar’s radiative luminosity, suggesting anisotropic or variable accretion.

Unified Astronomy Thesaurus concepts: [Intergalactic filaments \(811\)](#); [Circumgalactic medium \(1879\)](#); [Quasars \(1319\)](#); [Galaxy groups \(597\)](#)

1. Introduction

Observed scaling relations between the interstellar medium (ISM) and star formation in massive star-forming galaxies imply ISM depletion times of a few Gyr at low z (for a review, see Kennicutt & Evans 2012; see Leitner & Kravtsov 2011) and under 1 Gyr at $z > 1$ (e.g., Tacconi et al. 2013). These ISM depletion timescales are smaller than the age of the universe, indicating that galaxies must accrete gas from external reservoirs to enable future star formation and black hole growth. This fresh material can be supplied via mergers (e.g., Moreno et al. 2021), accretion of cool ($T \lesssim 10^5$ K) intergalactic/circumgalactic medium (IGM/CGM; e.g., Dekel et al. 2009), or cooling of hot ($T \gtrsim 10^6$ K) gaseous halos (e.g., Correa et al. 2018). Despite the importance of gas accretion in galaxy evolution, direct and unambiguous observations of accretion are rare (for a review, see Putman 2017).

The Milky Way represents a unique case where we can study gas accretion onto a galaxy over many phases and angles. The kinematics of the Milky Way’s extraplanar gas exhibit clear signs of accretion in both neutral and ionized phases (for a review, see Putman et al. 2012), with total inferred mass inflow rates consistent with the galaxy’s star formation rate (e.g., Lehner & Howk 2011).

Beyond the Milky Way, most studies of inflows rely on absorption features in galaxy spectra that are redshifted relative to the galaxy systemic velocity (for a review, see Rubin 2017). Despite the difficulty in detecting redshifted gas in “down-the-barrel” spectra, surveys at $z \lesssim 1.5$ have revealed likely inflows for ≈ 80 galaxies (e.g., Sato et al. 2009; Krug et al. 2010; Coil et al. 2011; Martin et al. 2012; Rubin et al. 2012). However, the locations of the inflowing gas relative to the galaxy are not directly constrained, leaving their origins and fate unknown.

In contrast, the background absorption spectroscopy often used to characterize the CGM (for reviews, see Chen et al. 2017; Tumlinson et al. 2017) informs the spatial distribution of the CGM and IGM around galaxies but carries little direct information on the radial direction of gas flows for individual systems. In rare cases, absorption spectroscopy can help



Original content from this work may be used under the terms of the [Creative Commons Attribution 4.0 licence](#). Any further distribution of this work must maintain attribution to the author(s) and the title of the work, journal citation and DOI.

differentiate inflows from outflows through modeling of velocity shear in multi-sight-line data (e.g., Chen et al. 2014; Lopez et al. 2018), detailed metallicity gradients (e.g., Fu et al. 2021), or correspondence with galactic rotation (e.g., Ho et al. 2017; Zabl et al. 2019), but all of these cases require model assumptions. Observations that carry direct information on both the morphology and radial direction of gas flows in the same systems have the potential to significantly improve our understanding of accretion onto galaxies.

Wide-field integral field spectrographs (IFSs) such as MUSE (Bacon et al. 2010) and KCWI (Martin et al. 2010) enable unprecedented morphological and kinematic maps of giant IGM/CGM nebulae through H I Ly α emission at $z \gtrsim 2$ (e.g., Cantalupo et al. 2014; Borisova et al. 2016; Cai et al. 2019; O’Sullivan et al. 2020; Chen et al. 2021; Fossati et al. 2021) and rest-frame NUV–optical emission features at lower redshift (Epinat et al. 2018; Johnson et al. 2018; Boselli et al. 2019; Chen et al. 2019; Rupke et al. 2019; Burchett et al. 2021; Helton et al. 2021; Zabl et al. 2021; Leclercq et al. 2022). At $z \lesssim 1$, IFSs provide highly complete galaxy redshift surveys and access to nonresonant emission lines to directly trace ionized gas morphology and kinematics. To date, IFS data enabled the discovery of halo-scale nebulae arising from large-scale outflows, cool intragroup medium, and stripping of ISM during galaxy interactions including two nebulae with additional insights from nearby intervening absorption spectroscopy (Chen et al. 2019; Zabl et al. 2021). Moreover, wide-field IFSs enable measurements of the velocity structure function that provide unique insights into turbulence in diffuse gas (e.g., Li et al. 2020; Chen et al. 2022). However, observations of gas accretion with wide-field IFSs remain ambiguous with the exception of a giant Ly α nebulae at $z = 3.3$ with evidence of infall coming from morphology (Rauch et al. 2011, 2016) and the Ly α emission profile (Vanzella et al. 2017).

Here, we report the emission detection of an accreting gas filament extending over >120 proper kpc (pkpc) from the halo into the ISM around TXS 0206–048, a luminous quasar at $z \approx 1$. An archival down-the-barrel UV spectrum of the quasar breaks the inflow/outflow degeneracy that limits intervening absorption studies and reveals inflowing absorption at velocities similar to the nearby nebular emission. The Letter proceeds as follows. In Section 2, we describe the MUSE, Hubble Space Telescope (HST), and Magellan observations and data reduction. In Section 3, we characterize the properties of TXS 0206–048 and its host group. In Section 4, we describe the giant nebulae in the quasar environment and the coincidence with inflowing gas seen in down-the-barrel absorption. In Section 5, we summarize our findings and discuss their implications. All magnitudes are given in the AB system. Throughout, we adopt a Λ cosmology with $\Omega_m = 0.3$, $\Omega_\Lambda = 0.7$, and $H_0 = 70 \text{ km s}^{-1} \text{ Mpc}^{-1}$.

2. Observations, Data Reduction, and Galaxy Measurements

Investigators studying the IGM and CGM (e.g., Tejos et al. 2014; Finn et al. 2016) obtained high-quality UV absorption spectra of TXS 0206–048 with the Cosmic Origins Spectrograph (COS; Green et al. 2012) due to its UV brightness, long redshift pathlength, and availability of archival data from the Gemini Deep Deep Survey (GDDS; Abraham et al. 2004). We obtained the COS G130M and G160M spectra of TXS 0206–048 (PI: Morris; PID: 12264) from MAST and

reduced them following procedures described in Johnson et al. (2013) and Chen et al. (2018) to improve the wavelength calibration.

The field near TXS 0206–048 was observed with the Advanced Camera for Surveys (ACS) on board HST with the F814W filter by the GDDS survey for a total of 32 ks (PI: Abraham; PID: 9760) and for 7.2 ks by a Sagittarius Stream program (PI: van der Marel; PID 12564), but the quasar falls just $4''$ from the edge of the field of view (FoV). To identify and measure the morphologies of faint galaxies near the quasar sight line, we obtained an additional 2.1 ks of exposure with ACS+F814W (PI: L. Straka; PID: 14660). We reduced and coadded the ACS imaging for the field using DrizzlePac (Hoffmann et al. 2021) including Tweakreg for alignment and Astrodrizzle to combine them. The effective wavelength of ACS+F814W corresponds to a rest-frame wavelength $\approx 3700 \text{ \AA}$ at $z = 1.13$.

To provide deep galaxy redshift survey data, we acquired a total of 8 hr of exposure under $0.''7$ seeing conditions on the field of TXS 0206–048 with MUSE as part of the MUSE-QuBES survey (PI: J. Schaye, PID: 094.A-0131, 094.A-0131). We reduced the data using the GTO pipeline (Weilbacher et al. 2014) and sky subtraction tools (Soto et al. 2016) as described in Johnson et al. (2018). To ensure robustness, we also reduced the MUSE data using CubEx (Borisova et al. 2016; Cantalupo et al. 2019) and the ESO pipeline (Weilbacher et al. 2020) and found consistent conclusions. We scaled the variance array reported by the GTO pipeline by a factor of 1.4 to better reflect empirical variance (see Herenz et al. 2017).

To detect faint emission near the quasar, we performed quasar light subtraction as described in Helton et al. (2021). We then identified galaxies in the MUSE FoV by running source extractor (Bertin & Arnouts 1996) on both the ACS image of the field and a median image formed from the MUSE data cube. Finally, we extracted spectra using MPDAF (Piqueras et al. 2017).

While the MUSE FoV is wide for an IFS, its FoV radius corresponds to a projected distance of $d = 250 - 350 \text{ pkpc}$ from the quasar at $z = 1.13$. We supplemented the MUSE data with a wider-field galaxy redshift survey using the LDSS3 spectrograph on Magellan following procedures outlined in Johnson et al. (2019). The LDSS3 FoV extends to $d \approx 1.5$ proper Mpc at the $z = 1.13$.

For both the MUSE and LDSS3 spectra, we measured redshifts by fitting the observed spectra with linear combinations of the first four galaxy eigenspectra from Bolton et al. (2012) as described in Johnson et al. (2018) and Helton et al. (2021). To prevent spatially coincident extended nebular emission from biasing galaxy redshifts, we measured galaxy redshifts based purely on stellar absorption when possible by masking strong emission lines. For galaxies without sufficient continuum signal-to-noise, we measured redshifts with the [O II] doublet. Finally, for galaxies with secure spectroscopic redshifts, we measured absolute magnitudes in the rest-frame B -band and 4000 \AA break strength ($D_n(4000)$; Balogh et al. 1999).

3. Quasar Properties and Environment

TXS 0206–048 is a luminous, core-dominated radio-loud quasar (Becker et al. 2001) at a redshift of $z = 1.1317 \pm 0.0002$ based on a measurement of the [O II] emission-line centroid in its MUSE spectrum and adopting the rest-frame effective [O II]

Table 1
Summary of Galaxies in the Field of TXS 0206–048 at $z \approx z_{\text{QSO}}$

ID	R.A. (J2000)	Decl. (J2000)	m_{F814W} (AB)	Redshift	Redshift Type	$\Delta\theta$ (arcsec)	d (pkpc)	Δv (km s ⁻¹)	$D_n(4000)$	M_B (AB)	$\log L_B/L_*$ ^a
quasar	02:09:30.77	-04:38:26.1	...	1.1317 ± 0.0002	[O II]	0.0	0	0
G1	02:09:30.42	-04:38:29.8	23.82 ± 0.02	1.1275 ± 0.0002	stellar	6.3	51	-590	1.31 ± 0.05	-20.4	-0.5
G2	02:09:30.92	-04:38:18.6	25.26 ± 0.08	1.1313 ± 0.0004	stellar	7.9	65	-60	1.13 ± 0.08	-18.9	-1.0
G3	02:09:30.59	-04:38:18.4	23.34 ± 0.03	1.1296 ± 0.0002	stellar	8.2	68	-300	1.06 ± 0.03	-20.6	-0.4
G4	02:09:31.35	-04:38:27.7	25.77 ± 0.13	1.1397 ± 0.0002	[O II]	8.8	72	+1130	1.17 ± 0.25	-18.4	-1.2
G5	02:09:30.14	-04:38:27.1	25.43 ± 0.09	1.1365 ± 0.0002	[O II]	9.3	77	+680	0.76 ± 0.21	-18.5	-1.2
G6	02:09:30.90	-04:38:15.5	24.26 ± 0.10	1.1295 ± 0.0002	stellar	10.8	89	-310	1.21 ± 0.07	-19.8	-0.7
G7	02:09:31.49	-04:38:21.1	23.68 ± 0.04	1.1287 ± 0.0002	stellar	11.9	98	-420	1.38 ± 0.07	-20.5	-0.4
G8	02:09:30.27	-04:38:16.6	24.93 ± 0.06	1.1300 ± 0.0002	[O II]	12.0	99	-240	1.02 ± 0.08	-19.0	-1.0
G9	02:09:30.95	-04:38:14.4	23.97 ± 0.05	1.1272 ± 0.0002	stellar	12.1	99	-630	1.32 ± 0.06	-20.2	-0.5
G10	02:09:31.01	-04:38:13.1	24.09 ± 0.06	1.1260 ± 0.0002	stellar	13.5	111	-800	1.23 ± 0.07	-20.1	-0.6
G11	02:09:31.48	-04:38:15.8	25.20 ± 0.09	1.1299 ± 0.0002	[O II]	14.9	122	-250	1.04 ± 0.10	-18.7	-1.1
G12	02:09:29.99	-04:38:15.7	25.53 ± 0.11	1.1305 ± 0.0002	[O II]	15.7	129	-170	1.03 ± 0.20	-18.4	-1.2
G13	02:09:31.80	-04:38:21.0	24.56 ± 0.08	1.1351 ± 0.0002	[O II]	16.3	134	+510	0.98 ± 0.09	-19.4	-0.9
G14	02:09:29.66	-04:38:25.1	24.13 ± 0.06	1.1271 ± 0.0002	stellar	16.6	137	-650	1.01 ± 0.10	-19.8	-0.7
G15	02:09:29.66	-04:38:26.0	25.04 ± 0.10	1.1232 ± 0.0002	[O II]	16.6	136	-1200	1.02 ± 0.16	-18.9	-1.0
G16	02:09:31.82	-04:38:34.0	25.23 ± 0.09	1.1264 ± 0.0002	[O II]	17.6	145	-750	0.90 ± 0.21	-18.7	-1.1
G17	02:09:30.39	-04:38:45.0	25.30 ± 0.10	1.1307 ± 0.0002	[O II]	19.6	161	-140	0.96 ± 0.13	-18.6	-1.2
G18	02:09:30.71	-04:38:47.6	24.46 ± 0.05	1.1299 ± 0.0002	[O II]	21.5	177	-250	1.02 ± 0.07	-19.5	-0.8
G19	02:09:29.44	-04:38:41.5	25.61 ± 0.07	1.1343 ± 0.0002	[O II]	25.1	206	+370	0.97 ± 0.28	-18.3	-1.3
G20	02:09:31.10	-04:38:00.5	23.18 ± 0.01	1.1368 ± 0.0002	stellar	26.1	215	+720	1.48 ± 0.04	-21.4	+0.0
G21	02:09:29.15	-04:38:43.5	23.17 ± 0.02	1.1259 ± 0.0002	stellar	29.8	244	-820	1.01 ± 0.03	-20.8	-0.3
G22	02:09:31.59	-04:38:54.4	23.42 ± 0.02	1.1331 ± 0.0002	stellar	30.8	253	+200	1.48 ± 0.05	-21.1	-0.1
G23	02:09:28.85	-04:38:41.1	23.36 ± 0.05	1.1259 ± 0.0002	stellar	32.4	266	-820	1.10 ± 0.04	-20.7	-0.3
G24	02:09:28.80	-04:38:40.6	25.04 ± 0.06	1.1345 ± 0.0002	[O II]	32.8	269	+390	0.93 ± 0.08	-18.9	-1.0
G25	02:09:31.16	-04:39:02.8	23.58 ± 0.03	1.1349 ± 0.0003	stellar	37.1	305	+450	1.47 ± 0.12	-21.0	-0.2
G26	02:09:28.29	-04:38:18.9	22.36 ± 0.01	1.1311 ± 0.0004	stellar	37.8	310	-80	1.40 ± 0.10	-22.2	+0.3
G27	02:09:30.95	-04:37:29.7	23.00 ± 0.03	1.1354 ± 0.0004	[O II]	56.5	465	+520	1.12 ± 0.21	-21.1	-0.2

Note.

^a We adopt an absolute magnitude of $M_B = -21.5$ for an L_* galaxy based on the luminosity function measurement from Faber et al. (2007). This corresponds to a luminosity of $\approx 5 \times 10^{10} L_\odot$.

doublet centroid and systemic uncertainty from Hewett & Wild (2010). To estimate the quasar’s luminosity and black hole mass, we fit the MUSE quasar spectrum near the Mg II emission line with a power-law continuum, Fe II template, and three Gaussian emission-line components using PyQSOFit (Guo et al. 2019). The measured monochromatic continuum luminosity at rest-frame 3000 Å implies a bolometric luminosity of $\log L_{\text{bol}}/\text{erg s}^{-1} \approx 47.2$ using bolometric corrections from Richards et al. (2006). The Mg II line width and luminosity result in an inferred black hole mass of $\log M_{\text{BH}}/M_\odot \approx 9.6$ using the single epoch virial theorem estimator from Shen et al. (2011).

To characterize the group environment of TXS 0206–048, we identified 27 galaxies in our spectroscopic survey with secure redshifts and velocities within ± 1500 km s⁻¹ of the quasar systemic redshift. Table 1 summarizes the properties of these galaxies including their R.A., decl., apparent magnitude in the F814W filter (m_{F814W}), redshift, redshift measurement type ([O II] emission or stellar absorption), projected angular ($\Delta\theta$) and physical distance (d) from the quasar sight line, line-of-sight velocity relative to the quasar (Δv), strength of the 4000 Å break ($D_n(4000)$), rest-frame B -band absolute magnitude (M_B), and B -band luminosity relative to L_* based on the $z = 1.1$ luminosity function from Faber et al. (2007).

To estimate the mass of the quasar host group, we measured the velocity dispersion of the group members including the quasar. We found a mean group velocity of $\Delta v_{\text{group}} = -130$

km s⁻¹ relative to the quasar and a velocity dispersion of $\sigma_{\text{group}} \approx 550$ km s⁻¹. Assuming that the group is relaxed, this line-of-sight velocity dispersion implies a dynamical mass of $\log M_{\text{dyn}}/M_\odot \approx 13.7$ using the cluster dispersion-to-mass relation from Munari et al. (2013). This is consistent with halo mass expectations based on the black hole mass of TXS 0206–048 and the black hole mass–halo mass relation inferred by Gaspari et al. (2019). The luminosity-weighted group center is ≈ 60 pkpc west and ≈ 20 pkpc north of the quasar assuming the quasar host has a luminosity of $L_B = 1 - 3 L_*$, which is typical of luminous active galactic nuclei (AGN; e.g., Zakamska et al. 2006). The location of the luminosity-weighted group center is driven away from that of the quasar primarily by one luminous galaxy, G26, which falls outside of the MUSE FoV. The MUSE galaxy redshift survey is deeper than the LDSS3 survey, so the group center may be biased toward the center of the MUSE FoV. A full image of the group is included in the Appendix.

4. Giant Nebulae around TXS 0206–048

At the redshift of TXS 0206–048, the [O II] $\lambda\lambda$ 3727, 3729 doublet, which traces cool ($T \sim 10^4$ K) ionized gas, is observed at ≈ 7940 Å. To identify [O II] emitting nebulae around the quasar, we performed continuum subtraction on the quasar-light-subtracted MUSE data cube by fitting low-order polynomials to each spaxel over a wavelength interval of

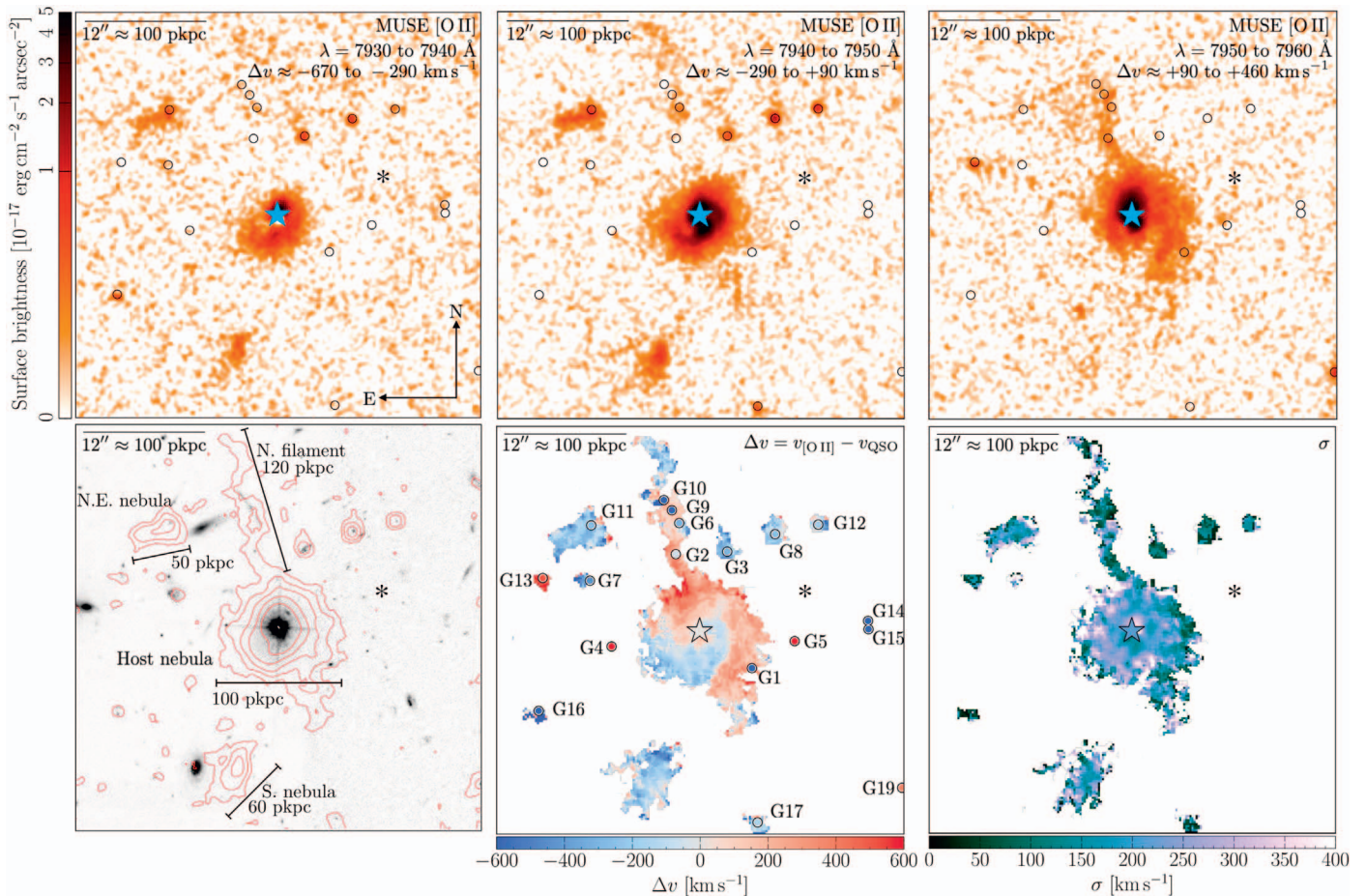


Figure 1. Top panels: continuum-subtracted, narrowband images around the [O II] doublet with wavelength ranges chosen to highlight nebulae in the environment of TXS 0206–048. The wavelength range and corresponding approximate [O II] line-of-sight velocity relative to the quasar systemic are labeled in the top right corner of each panel. In each panel, the locations of galaxies in the quasar host environment are marked with black circles and the quasar position is marked by a star. Bottom left panel: [O II] surface brightness contours overlaid on the HST ACS/F814W image of the field marking surface brightness levels of 0.15, 0.3, 0.6, 1.2, and $2.4 \times 10^{-17} \text{ erg s}^{-1} \text{ cm}^{-2} \text{ arcsec}^{-2}$ after smoothing with a $1'' \times 1''$ boxcar. The [O II] contours are formed by summing the three images in the top panels. Bottom middle and right panels: [O II] line-of-sight velocity and line-of-sight velocity dispersion maps of the nebulae around TXS 0206–048 calculated with doublet fitting as described in the text. The locations of group members (quasar) are marked by black circles (black star) in the middle panel and the color interior to the symbols shows the objects systemic line-of-sight velocity relative to the quasar, Δv . The approximate luminosity-weighted group center is marked with an asterisk in all panels.

7800–8100 Å after masking the 50 Å region around [O II]. We then subtracted the continuum fit from each spaxel to produce an emission-line data cube with a typical 3σ detection limit of $10^{-18} \text{ erg s}^{-1} \text{ cm}^{-2} \text{ arcsec}^{-2}$ for a line with a width $\sigma = 200 \text{ km s}^{-1}$ averaged over an $r = 0''.5$ aperture.

The continuum-subtracted data cube reveals the presence of four distinct, 50–100 pkpc scale ionized nebulae emitting in [O II] in the quasar host group and several smaller-scale nebulae closely associated with group members. To visualize these nebulae, the top three panels of Figure 1 display continuum-subtracted [O II] surface brightness maps integrated over three 10 Å intervals that correspond to line-of-sight velocities of $\Delta v \approx -670$ to -290 , -290 to 90 , and 90 to 460 km s^{-1} relative to the quasar systemic velocity. We note that the [O II] doublet separation corresponds to $\approx 200 \text{ km s}^{-1}$ so this velocity correspondence is approximate. Throughout the Letter, we refer to these nebulae by their morphology and location relative to the quasar as the Northeast (NE) nebula, the South (S) nebula, the North (N) filament, and the Host nebula (see Figure 1). In addition to these, there is a possible second filamentary feature extending south of the Host nebula seen in

Figure 1. However it is less prominent than the N filament and may be an extension of the Host nebula’s arm-like feature.

To visualize the morphologies of the nebulae relative to galaxies in the group, the bottom left panel of Figure 1 displays the HST image of the field overlaid with [O II] surface brightness contours computed from the sum of the three images shown in the top three panels. The nebulae are labeled by their name and approximate length scale in the bottom left panel. To better quantify the kinematics of these nebulae, we also performed [O II] doublet fitting to the data cube as described in Johnson et al. (2018) and Helton et al. (2021). The bottom middle and bottom right panels of Figure 1 display the line-of-sight velocity relative to the quasar and line-of-sight velocity dispersion (corrected for the MUSE line spread function Bacon et al. 2017), respectively. In most cases, the emission is too broad or too low in signal-to-noise ratio (S/N) to measure the [O II] 3729-to-3727 doublet ratio, which can vary between 0.35 and 1.5. Uncertainty in the doublet ratio introduces a systematic uncertainty of ≈ 50 – 80 km s^{-1} in the [O II] velocity centroid. Table 2 summarizes the properties of the nebulae, and we discuss each in turn in the following.

Table 2
Summary of Properties of the Nebulae around TXS 0206–048

Name	$\Delta\theta$ (arcsec)	d (pkpc)	Δv (km s ⁻¹)	σ (km s ⁻¹)	Length Scale (pkpc)	Area (pkpc ²)	[O II] Surface Brightness ^a (erg s ⁻¹ cm ⁻² arcsec ⁻²)	[O II] Flux ^a (erg s ⁻¹ cm ⁻²)	[O II] Luminosity ^a (erg s ⁻¹)
NE nebula	15.0	120	-240	180	50	900	0.1 to 1.0×10^{-17}	5.1×10^{-17}	3.6×10^{41}
S nebula	15.0	120	-250 to -110	170	60	1100	0.1 to 1.0×10^{-17}	5.8×10^{-17}	4.1×10^{41}
N filament	6.0–20.5	50–170	-250 to +330	100–230	120	2000	0.1 to 0.3×10^{-17}	5.4×10^{-17}	3.8×10^{41}
Host nebula	0–6	0–50	-300 to +540	100–300	100	6800	0.1 to 24.3×10^{-17}	1.2×10^{-15a}	8.5×10^{42}

Note.

^a The total fluxes and luminosities are integrated within isophotal areas with surface brightness greater than 10^{-18} erg s⁻¹ cm⁻² arcsec⁻². For the Host nebula, we masked a circular region with radius $r = 1''$ when measuring the total [O II] flux and luminosity to avoid large residuals from the quasar subtraction. If this region is not masked, the measured flux and luminosity increase by a factor of 2.

4.1. Northeast Nebula

The NE nebula is located $\Delta\theta \approx 15''$ or $d \approx 120$ pkpc from TXS 0206–048 and has a length scale of ≈ 50 pkpc and [O II] surface brightness ranging from ≈ 0.1 to 1.0×10^{-17} erg s⁻¹ cm⁻² arcsec⁻². The NE nebula exhibits a head–tail morphology oriented approximately east–west with a surface brightness peak that is spatially coincident with a group member galaxy, G11. Together, the morphology and spatial coincidence with G11 suggest that the NE nebula arises from ram pressure stripping of the ISM of G11 as it moves through the hot halo of the quasar host group. Such “jellyfish” galaxies are often observed in galaxy clusters and groups (e.g., Fumagalli et al. 2014; Poggianti et al. 2017; Boselli et al. 2019; Chen et al. 2019) and around quasar hosts at $z \approx 0.5$ (e.g., Johnson et al. 2018; Helton et al. 2021) where tidal stripping also plays a role (see also Decarli et al. 2019, for a case of likely tidal stripping around a quasar at $z = 6$). We caution that the continuum S/N of G11 is too low to measure a stellar-absorption-based redshift.

4.2. South Nebula

The S nebula is located $\Delta\theta = 15''$ or $d \approx 120$ pkpc south of TXS 0206–048, extends over a length scale ≈ 60 pkpc, and exhibits [O II] surface brightness of ≈ 0.1 to 1.0×10^{-17} erg s⁻¹ cm⁻² arcsec⁻². While the surface brightness contours of the S nebula are somewhat elongated, its surface brightness peak is not coincident with any continuum sources in the HST image. At the location of the S nebula, the HST image is sensitive to galaxies of $M_B = -16$ at $z = 1.13$. The morphology and lack of associated galaxies suggest that the S nebula is a collection of cool intragroup medium clouds in the massive halo (e.g., Nelson et al. 2020), similar to others observed around quasars (e.g., Johnson et al. 2018; Helton et al. 2021) at $z \approx 0.5$. However, we note that the S nebula could also represent ram pressure debris stripped from the ISM of a dwarf galaxy fainter than $L_B \approx 0.006L_*$. The brightest galaxy without a robust redshift near the S nebula falls along the northern edge of faintest [O II] surface brightness contour shown in the bottom left panel of Figure 1. This galaxy has an apparent magnitude of $m_{F814W} = 26.0$ that would correspond to an absolute magnitude of $M_B = -18.1$ at $z = 1.13$, but it lacks the strong nebular emission expected from a galaxy experiencing ongoing ram pressure stripping.

4.3. North Filament

The N filament extends from $\Delta\theta \approx 20''/5$ or $d = 170$ pkpc north of the quasar toward it and intersects with the Host nebula $6''$ or $d = 50$ pkpc from the quasar. Despite its length, the N filament is narrow with a width that ranges from $1''$ to $3''$ or ≈ 8 to 24 pkpc. The N filament is fainter than the other nebulae in the field with a peak [O II] surface brightness of 0.3×10^{-17} erg s⁻¹ cm⁻² arcsec⁻². The kinematics of the N filament are complex, and vary from $\Delta v \approx -250$ km s⁻¹ at its northernmost points to $\Delta v \approx +350$ km s⁻¹ where it intersects with the Host nebula. The N filament is spatially coincident with nearby galaxies, extending ≈ 30 pkpc to the north of G10 and connecting G9, G6, and G2 before intersecting with the Host nebula. Kinematically, the velocity of the N filament appears distinct from G2, G6, G9, and G10 but matches that of the Host nebula where they intersect, as seen in Figure 1.

Optically emitting outflows from radio-loud AGN are commonly observed with orientations aligned with radio lobes (e.g., Nesvadba et al. 2017), which could explain the morphology of the N filament. However, these outflows typically exhibit broad line widths of $500 < \text{FWHM} < 1500$ km s⁻¹ while the N filament exhibits a median width of $\text{FWHM} \approx 300$ km s⁻¹. Furthermore, radio observations from FIRST (Becker et al. 2001), VLASS (Lacy et al. 2020), and the XXL Survey GMRT 610 MHz continuum observations (Smolcic et al. 2018) reveal no evidence of a jet or lobe aligned with the N filament despite 3σ detection limits of 450, 210, and 140 μJy per beam, respectively. Starburst-driven outflows and radio-quiet AGN-driven outflows typically exhibit wide opening angles (e.g., Liu et al. 2013; Rupke et al. 2019; Burchett et al. 2021; Zabl et al. 2021) inconsistent with the morphology of the N filament. Together, the kinematics, morphology, and lack of detected jets disfavor an outflow origin for the N filament.

The morphology of the N filament can be explained if it arises from overlapping nebulae resulting from ongoing ram pressure stripping of group members or cool, filamentary accretion. The ongoing ram pressure stripping scenario can explain the spatial coincidence with galaxies but would require a somewhat contrived chance alignment. Further, the significant differences between the [O II] emission velocities of the nebulae versus stellar absorption velocities of galaxies G2, G6, G9, and G10 disfavors ongoing stripping of ISM. To quantify the velocity differences, Figure 2 displays the [O II]-based velocities for the N filament and the stellar absorption-based velocities of G2, G6, G9, and G10 versus projected distance

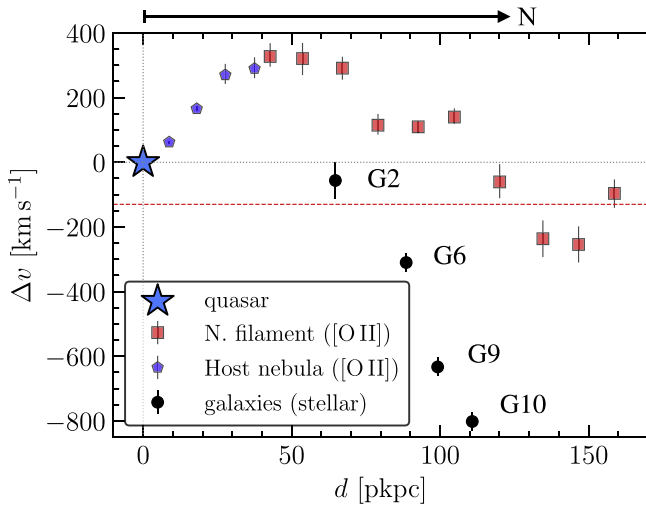


Figure 2. Line-of-sight velocity of the Host nebula and N filament as a function of projected distance from the quasar compared with nearby galaxies. Points corresponding to the Host nebula are shown as blue pentagons and those corresponding to the N filament are shown as red squares. The N filament measurements are made following the filament contours seen in Figure 1 with $0''.6$ – $1''.2$ radius extraction apertures depending on the width of the filament at each location. The measurements for the Host nebula are made moving north from the quasar toward the N filament with $0''.6$ radius extractions. Galaxies G2, G6, G9, and G11 overlap spatially with the N filament and their stellar velocities vs. projected distances are shown in black circles in the bottom panel for comparison with the nebulae the quasar marked by a blue star. Despite their spatial coincidence seen in Figure 1, the line-of-sight [O II] velocities of the N filament differ from nearby galaxies by $\gtrsim 300 \text{ km s}^{-1}$. The luminosity-weighted group velocity is indicated by the red dashed line.

from the quasar. The galaxy and nebular line-of-sight velocities differ by more than 300 km s^{-1} , even at the locations of the galaxies. This mismatch is inconsistent with previous observations of nebulae arising from ongoing ram pressure stripping of ISM (Johnson et al. 2018; Boselli et al. 2019; Chen et al. 2019; Helton et al. 2021).

The long, narrow morphology, lack of kinematic correspondence with galaxies, and matching velocity to the northern edge of the Host nebula all suggest the N filament arises from cool, filamentary accretion. Such cool accretion could result from several mechanisms including (1) a cooling flow from the hot halo of the quasar host group, (2) cool, filamentary gas accreting from the IGM, or (3) accreting cool CGM and intragroup medium from a less massive galaxy group as it falls into the quasar host system. Filamentary cooling flows in cool-core clusters are observed in optical emission lines including [O II] (e.g., McDonald et al. 2010, 2012). In this case, the N filament would be the longest and highest redshift known in such flow despite arising in a less massive system with a velocity dispersion $\approx 3\times$ lower than that of the current record holder, the Phoenix Cluster (McDonald et al. 2012). Spatial coincidence with group members is not typical for cooling flows in cool-core clusters. Instead, the filament could represent chaotic cold accretion from the hot halo (e.g., Gaspari et al. 2018) if interactions between G2, G6, G9, G10, and the quasar host induce turbulent cooling. In this case, the complex velocity shear would reflect bulk motion of the hot halo.

Alternatively, the N filament’s morphology and coincidence with galaxies can be explained by cool accretion of an intergalactic medium filament connecting galaxies G2, G6, G9, and G10 or CGM from a galaxy group containing G2, G6, G9, and G10 as the group is accreted by the quasar host system. In

both cases, the velocity difference between the nebulae and nearby galaxies can be explained if the gas experienced ram pressure deceleration over sufficiently long timescales. Bulk motion of hot halos can include rotation (e.g., Hodges-Kluck et al. 2016; Oppenheimer et al. 2018) or other complex patterns that could explain the velocity shear of the N filament. The accreting CGM scenario would require tidal forces to explain the elongated morphology.

An IGM filament would explain the morphology and potentially connect galaxies. The ratio of the stream minor axis radius to the estimated host halo virial radius ($\approx 560 \text{ pkpc}$) is $\approx 1\%$ – 4% , consistent with predictions for cool inflowing IGM streams from Mandelker et al. (2020). The N filament’s properties can also be explained by CGM or intragroup medium in the presence of interactions. In particular, if the filament originated as CGM or intragroup medium around G2, G6, G9, and G10, the elongated morphology could be the result of tidal and ram pressure forces experienced as the group members and surrounding gas fell toward the quasar host. In summary, the morphology and kinematics of the N filament are consistent with cool filamentary accretion from the IGM, from the CGM/intragroup medium around a group of galaxies being accreted by the quasar host system, or interaction-induced cooling of hot gas.

4.4. Host Nebula

The Host nebula is approximately centered on the quasar and extends to a radius of $\Delta\theta = 6''$ or $d \approx 50 \text{ pkpc}$ from the quasar with [O II] surface brightness levels ranging from 0.1 to $24 \times 10^{-17} \text{ erg s}^{-1} \text{ cm}^{-2} \text{ arcsec}^{-2}$. The kinematics of the Host nebula are complex with line-of-sight velocities ranging from ≈ -300 to $+540 \text{ km s}^{-1}$ and distinct spiral-like structure seen in Figure 1.

The radial extent, morphological correspondence with the quasar, and high peak surface brightness suggest that the Host nebula represents extended, ionized ISM and diffuse gas around the quasar host. However, the Host nebula’s kinematics are more complex than the canonical “spider” diagram expected for rotating disks. Quantitative analysis of the velocity structure function of the Host nebula demonstrates that it follows expectations for Kolmogorov turbulence with isotropic, homogeneous, and incompressible gas (see Chen et al. 2022).

The unusual spiral structure visible in the surface brightness panels (top) and velocity map (bottom middle) in Figure 1 may be a signature of tidal arms from a past interaction, possibly one that helped fuel the quasar. However, the bright quasar limits our ability to search for interaction signatures that would confirm this scenario.

To investigate whether there is a significant, large-scale inflow or outflow associated with the Host nebula, we take advantage of the archival COS spectrum of the quasar, which enables clean differentiation of outflowing (blueshifted) and inflowing (redshifted) gas along the quasar sight line. The COS spectrum reveals narrow associated absorption, including both outflowing and inflowing components detected in an array of ions. The middle and bottom panels on the right of Figure 3 show O V $\lambda 629$ and N IV $\lambda 569$ absorption as a function of line-of-sight velocity relative to the quasar. Finn et al. (2014) conducted ionization analysis of these absorbers and found that the absorbing clouds likely arise at distances of $\gtrsim 2 \text{ pkpc}$ from the nucleus. This is only slightly smaller than the angular resolution of the seeing limited MUSE data ($0''.7$ corresponds

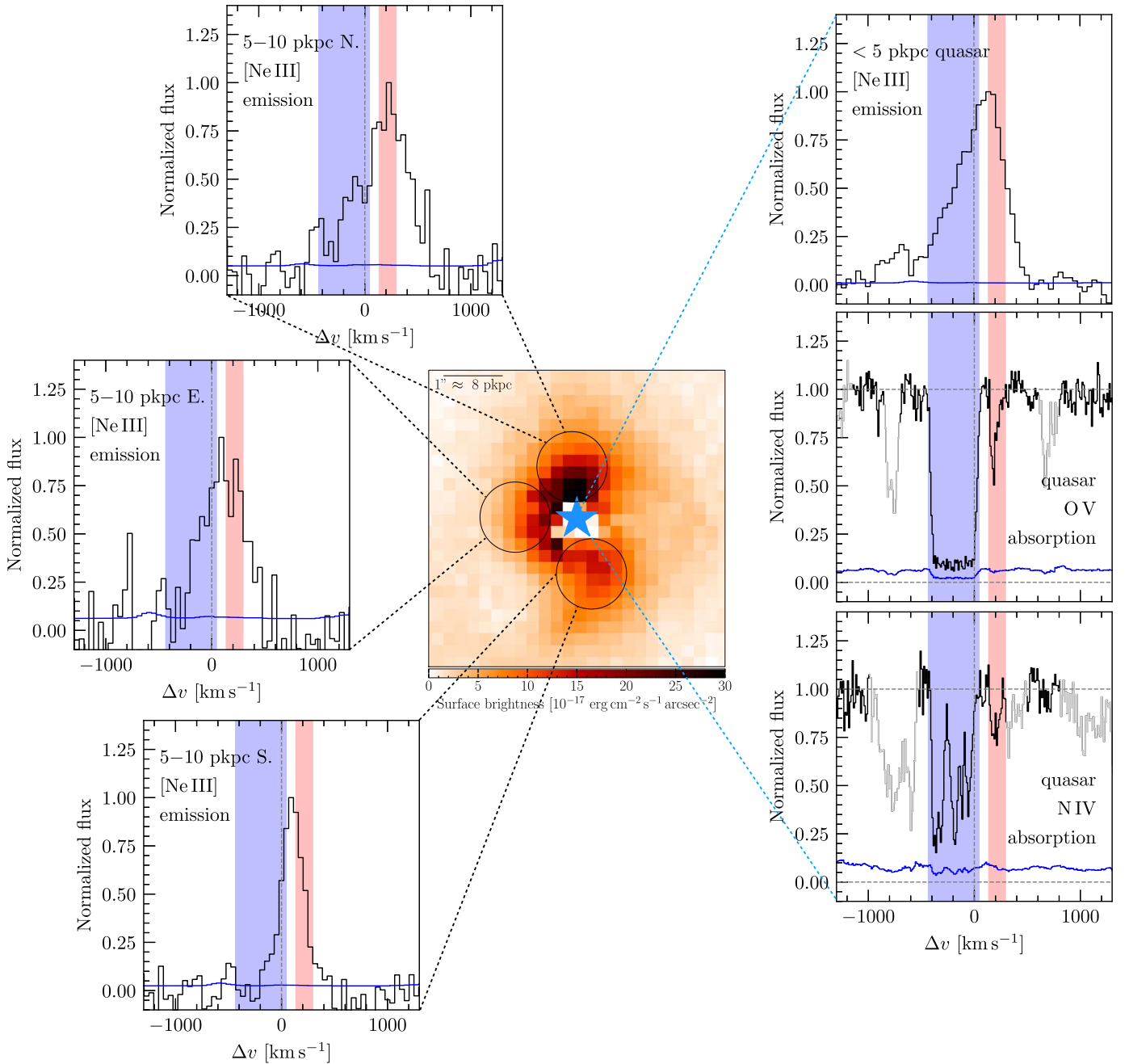


Figure 3. Summary of emitting and absorbing gas kinematics near the nucleus. The image in the center panel displays the [O II] surface brightness map zoomed in and scaled to highlight structures near the nucleus. The quasar position is marked by a blue star and pixels touching the star are subject to large uncertainties in quasar light subtraction. The top right panel shows normalized flux of [Ne III] vs. line-of-sight velocity from the quasar while the three panels on the left display [Ne III] emission for circular apertures offset from the quasar centroid. The regions corresponding to each spectrum are shown in black circles and connected to the corresponding spectral panel by a dashed black line. The bottom two panels on the right display O V (middle right) and N IV (bottom right) narrow, associated absorption from the COS FUV spectrum of TXS 0206–048. The COS spectrum reveals both outflowing (blueshifted) and inflowing (redshifted) absorption and photoionization analysis of the absorbers from Finn et al. (2014), indicating that the absorbing gas arises at distances of 2–6 pkpc from the nucleus. For reference, the velocity ranges of the outflowing and inflowing material observed in the quasar absorption spectrum are shown in blue and red highlighting, respectively. The inflowing component exhibits a line-of-sight velocity of $\approx +200$ km s $^{-1}$ that is consistent with the velocity field seen in [Ne III] emission seen at 5–10 kpc from the quasar in the panels on the left. The outflowing absorbing gas shows velocities that are comparable to the nuclear [Ne III] but exceed the blueshifts seen in emission at $d = 5$ –10 kpc seen in the left three panels.

to ≈ 6 pkpc at $z = 1.13$), providing a unique opportunity to jointly study the emitting and absorbing gas near the quasar.

The regions of the Host nebula near the quasar are bright enough to be observed in [Ne III] $\lambda 3869$ emission, which enables more precise velocity measurements. To search for kinematic correspondence between the emitting gas and

associated absorbers, Figure 3 displays peak-normalized [Ne III] emission as a function of line-of-sight velocity for a central ($d < 5$ pkpc) extraction centered on the quasar in the top right panel and extractions at $d = 5$ –10 pkpc immediately to the N (top left panel), E (middle left panel), and S (bottom left panel).

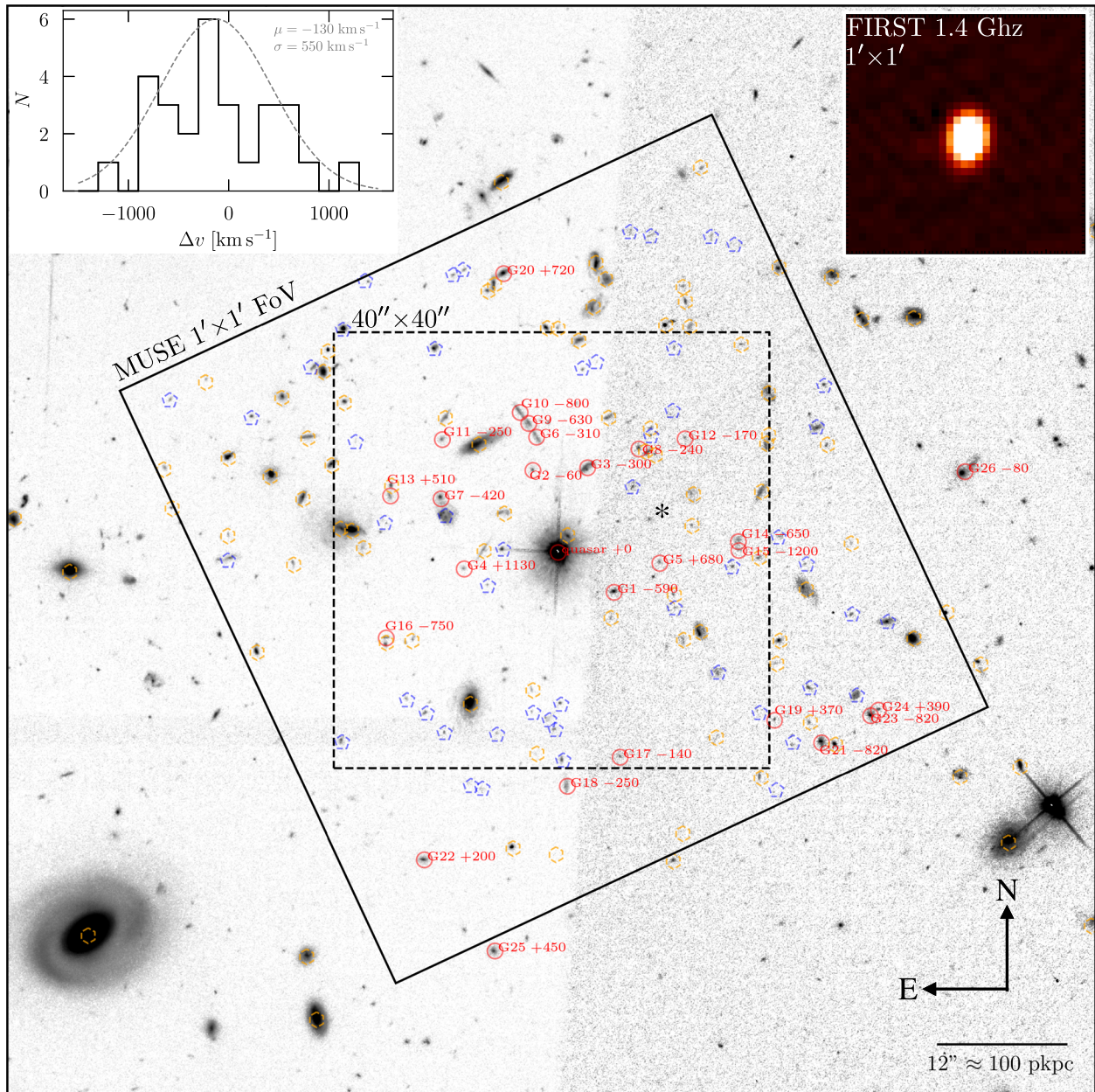


Figure 4. Summary of the redshift survey and galaxy group hosting TXS 0206–048. The grayscale image displays the reduced, coadded HST ACS+F814W image of the field centered on TXS 0206–048 with orientation and scale marked at the bottom right. The full $1' \times 1'$ MUSE FoV is marked by the black square with solid outline, and the $40'' \times 40''$ region shown in Figure 1 is marked with a dashed line. Galaxies in the group hosting TXS 0206–048 are labeled with red circles and labeled by their ID and velocity in km s^{-1} from Table 1. The approximate luminosity-weighted group center is marked with an asterisk. Galaxies with secure redshifts but foreground and background to the quasar host group are marked with blue and orange dashed symbols, respectively. The inset panel at the top left displays the line-of-sight velocity histogram for group members, including TXS 0206–048, with a black, solid line, while the best-fitting Gaussian with a mean line-of-sight velocity of $\mu = -130 \text{ km s}^{-1}$ and a line-of-sight velocity dispersion of $\sigma = 550 \text{ km s}^{-1}$ is shown with a dashed gray line. The 1.4 GHz radio image from the FIRST survey is shown in the top right inset panel and confirms the core-dominated nature of this radio-loud quasar.

The [Ne III] emission at $d < 5 \text{ pkpc}$ from the quasar sight line peaks between the quasar systemic velocity and that of the inflowing component seen in associated absorption in O V, N IV, and other ions. The circumnuclear [Ne III] emission also exhibits a prominent blue wing extending from $\Delta v \approx -200$ to -400 km s^{-1} , similar to the outflowing absorbers. The similarity in velocity range observed between the associated inflow/outflow observed in absorption and the circumnuclear [Ne III] suggests that the emissions may trace different phases and locations of the the same gas flows traced in absorption.

Further from the nucleus, the [Ne III] emission at $d = 5 - 10 \text{ pkpc}$ shows decreased prominence of the blue wing, suggesting that the faster outflow component at $\Delta v < -200 \text{ km s}^{-1}$ may be confined to central regions of the host. On the other hand, the redshifted emission component is more prominent and peaks near the associated inflow velocity, particularly in the N extraction. The more extended nature of the redshifted emission and kinematic coincidence with the associated inflow suggest a common origin and a relation to Host nebulae. In this case, the emitting gas near the nucleus would have to be in front of the

quasar and oriented toward us within the quasar ionizing radiation cone to be illuminated and for the line-of-sight velocity to approximately match the radial velocity of the down-the-barrel inflow.

5. Discussion and Conclusions

Based on a combination of deep MUSE observations and archival HST data, we discovered four distinct and giant ionized nebulae in the environment of TXS 0206–048, a luminous quasar at $z = 1.13$. Some of these nebulae are likely related to an inflow detected in UV absorption. Two of the nebulae are well separated from the quasar host galaxy and likely arise from ongoing ram pressure stripping of a group member (NE nebula) and cool clouds in the intragroup medium (S nebula), extending observations of large-scale streams observed in groups and around quasar hosts to higher redshift (e.g., Hess et al. 2017; Johnson et al. 2018; Helton et al. 2021).

The two other giant nebulae include a ≈ 120 pkpc filament extending to the N of the quasar (N filament), which intersects—both spatially and kinematically—with a 100 pkpc diameter nebula (Host nebula) surrounding the quasar host itself. Immediately around the quasar, the Host nebula exhibits velocities similar to inflowing absorbing gas observed in UV spectra of the quasar. The morphology and kinematics of the N filament and Host nebula and coincidental inflowing gas constitute strong evidence of large-scale, cool filamentary accretion from halo scales into the quasar host and toward the nucleus.

If the [O II] emitting gas is in pressure equilibrium with a hot halo, we can gain insights into its physical conditions. Hydrodynamical simulations predict global pressure equilibrium, although small-scale fluctuations from subsonic turbulence can occur (e.g., van de Voort & Schaye 2012; Gaspari et al. 2014), though observational results are mixed (see Werk et al. 2014; Stern et al. 2016; Zahedy et al. 2019; Butsky et al. 2020; Qu et al. 2022). Adopting the group mass from Section 3 and the generalized Navarro–Frenk–White (NFW) pressure profile from Arnaud et al. (2010), we estimate hot halo pressure of $P_{\text{hot}}/k_B \approx 5 \times 10^4 \text{ K cm}^{-3}$ at ≈ 100 pkpc for the N filament. Based on Cloudy v17.03 (Ferland et al. 2017) photoionization equilibrium models for gas illuminated by the quasar that dominates over the expected UV background at these distances (e.g., Faucher-Giguere 2019), we expect a temperature of $\log T/\text{K} = 4 - 4.5$ and a density of $n_e \approx 1 - 5 \text{ cm}^{-3}$.

Estimating the surface brightness of [O II] given a density and total ionized column, $N(\text{H II})$, is complicated by the unknown ionization state and metallicity of the gas. However, we expect a line ratio of [O II]/ $\text{H}\alpha \sim 1$ over a fairly wide range of conditions for AGN photoionized gas (e.g., Groves et al. 2004), enabling us to roughly estimate the ionized gas column because $\text{H}\alpha$ surface brightness can be approximated as $\text{SB}_{\text{H}\alpha} \approx 1.7 \times 10^{-16} C \left(\frac{n_e}{\text{cm}^{-3}} \right) \left(\frac{N(\text{H II})}{3 \times 10^{20} \text{ cm}^{-2}} \right) \left(\frac{1}{1+z} \right)^4$ $\text{erg s}^{-1} \text{ cm}^{-2} \text{ arcsec}^{-2}$ where C is the clumping factor, $C = \langle n_e^2 \rangle / \langle n_e \rangle^2$. Assuming $n_e \sim 3 \text{ cm}^{-3}$ and $C \approx 1$, the surface brightnesses of the N filament corresponds to approximate ionized gas columns of $N(\text{H II}) \sim 10^{19} \text{ cm}^{-2}$. With the same assumptions, we estimate total ionized gas masses of $M_g \sim 10^9$ and $2 \times 10^{10} M_\odot$ for the N filament and Host nebula, respectively, based on the total line luminosity following Greene et al. (2011). These are significantly lower than the estimates of ionized gas mass assuming the same density and

near unity volume filling factor that results in $M_{\text{gas}} \sim 10^{12} M_\odot$ for the N filament assuming a cylinder with length of $l = 100$ pkpc and radius of $r = 10$ pkpc and $M_{\text{gas}} \sim 10^{13} M_\odot$ for the Host nebula assuming a uniform sphere with radius $r = 50$ pkpc. These volume-based estimates significantly exceed not only the previous luminosity-based estimates but also the expected baryon budget for the group, requiring lower mean density and higher clumping factor (e.g., Cantalupo et al. 2019). With a clumping factor of $C \approx 100$, the discrepancy between the two mass estimates can be resolved. Insights into the density structure of the gas require new emission observations.

Given its low surface brightness and possible column density, the N filament may arise in gas analogous to Lyman limit systems and damped $\text{Ly}\alpha$ absorbers but in a more overdense, higher-pressure environment and subjected to intense ionizing radiation from the quasar. The $\approx 80 \times$ higher peak surface brightness of the inner regions of the Host nebula suggests significantly higher density or ionized gas column, consistent with ISM. The inflowing absorption detected in the spectrum of TXS 0206–048 combined with the morphology of the extended, emitting gas of the Host nebula provides an opportunity to estimate the accretion rate in a quasar host assuming that the absorbing gas and extended emission are tracing different phases and locations along a coherent gas flow. Following Weiner et al. (2009), we assume a thin, spherical shell that results in an inflow rate of $\frac{dM}{dt} \sim (22 M_\odot \text{ yr}^{-1}) \left(\frac{N(\text{H})}{10^{20} \text{ cm}^{-2}} \right) \left(\frac{R}{5 \text{ pkpc}} \right) \left(\frac{v}{300 \text{ km s}^{-1}} \right)$ where $N(\text{H})$ is the total hydrogen column density of the inflow, R is the radius of the shell, and v is the inflow velocity. While it is an oversimplification, we chose the thin shell for ease of comparison with previous results (e.g., Arav et al. 2013) and to place a conservative upper limit on the inflow rate. Adopting a uniform, spherical flow of radius R would reduce the inflow rate by a factor of 3. With a total column of $N(\text{H}) \sim 10^{17} \text{ cm}^{-1}$ based on the ionization analysis of Finn et al. (2014), a radius of $R < 50$ pkpc based on the maximum observed extent of the Host nebula, and the observed inflow velocity of $v \approx 150 \text{ km s}^{-1}$, we infer an upper limit on the inflow rate of $\frac{dM}{dt} < 0.1 M_\odot \text{ yr}^{-1}$. The inflowing absorbing gas column inferred by Finn et al. (2014) is several orders of magnitude below our initial surface-brightness-based estimate for the ionized column. This can be resolved if the emitting gas traces denser, higher column density gas phase with lower covering factor than the absorbing gas or equivalently, by a clumping factor of ≈ 100 as previously suggested. The HI column for the inflow inferred by Finn et al. (2014) is based on metal absorption only and assumes approximately solar metallicity due to unavailability of an HI column measurement.

If the absorbing gas arises closer to the nucleus at ≈ 2 pkpc (Finn et al. 2014), then the inflow rate estimate decreases to $\frac{dM}{dt} < 0.004 M_\odot \text{ yr}^{-1}$. An inflow rate of $0.1 M_\odot \text{ yr}^{-1}$ corresponds to a luminosity of $\sim 5 \times 10^{45} \text{ erg s}^{-1}$ or a radiative luminosity of $\sim 5 \times 10^{44} \text{ erg s}^{-1}$ assuming a radiative efficiency of 10%. This is several orders of magnitude below the observed radiative luminosity of the quasar indicating a significant difference in accretion rate at $\gtrsim 2$ pkpc compared to nearer the accretion disk. This large difference suggests highly anisotropic or highly time variable accretion. Time variable accretion will be reflected in luminosity variability of the quasar, though we note that TXS 0206–048 exhibits 5% level variability in the UV on month timescales (e.g., Punsly et al. 2016). Accretion

mechanisms such as chaotic cold accretion (e.g., Gaspari et al. 2018) and interaction-induced quasar activity (e.g., Goulding et al. 2018) are expected to produce significant accretion rate variability on timescales comparable to the dynamical time at a few proper kiloparsecs. Alternatively, the observations of accretion rate at $\gtrsim 2$ pkpc than is orders of magnitude lower than that inferred for the quasar engine itself on much smaller scales could be a signature of effective AGN feedback heating the CGM to slow accretion.

The discovery and morphokinematic analysis of multiple large nebulae including a ≈ 100 pkpc long filament and connected ≈ 100 kpc diameter nebulae around a luminous quasar with an inflowing associated absorber demonstrate the unique insights enabled by observations of nonresonant emission lines with wide-field IFSs when coupled with down-the-barrel absorption spectroscopy. Developing a better understanding of the origins, fate, and physical conditions of these gas flows requires observations of emission lines from a wider variety of ions, which will become possible with upcoming near-IR IFSs such as MIRMOS on Magellan (Konidaris et al. 2020) and HARMONI (Thatte et al. 2021) on the E-ELT.

The authors are grateful for the efforts of the anonymous referee whose thorough feedback strengthened the paper. S.D.J. gratefully acknowledges partial support from HST-GO-15280.009-A, HST-GO-15298.007-A, HST-GO-15655.018-A, and HST-GO-15935.021-A. M.G. acknowledges partial support by HST-GO-15890.020/023-A, the *BlackHoleWeather* program, and NASA HEC Pleiades (SMD-2359). S.C. gratefully acknowledges support from the European Research Council (ERC) under the European Unions Horizon 2020 research and innovation program grant agreement No. 864361. G.L.W. acknowledges partial support from HST-GO-15655.006-A and HST-GO-16016.002.

Based on observations from the European Organization for Astronomical Research in the Southern Hemisphere under ESO (PI: Schaye, PID: 094.A-0131) and the NASA/ESA Hubble Space Telescope (PI: Abraham, PID: 9760; PI: Morris, 12264; PI: van der Marel, PID: 12564; PI: L. Straka; PID: 14660). The COS spectra and ACS images analyzed in this paper can be accessed via COS doi:10.17909/4dnz-y880 and ACS doi:10.17909/tekk-dx10, respectively.



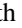
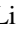




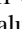
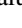
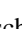
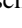
This Letter includes data gathered with the 6.5 m Magellan Telescopes located at Las Campanas Observatory, Chile. The paper made use of the NASA/IPAC Extragalactic Database, the NASA Astrophysics Data System, Astropy (Astropy Collaboration et al. 2018), and Aply (Robitaille & Bressert 2012).

Appendix

Supplemental Information on the Group Hosting TXS 0206–048

To provide additional context on the galaxy group hosting TXS 0206–048, Figure 4 displays a wider FoV version of the HST ACS+F814W image with galaxies labeled by group membership based on spectroscopic redshifts as described in Section 3. The figure also highlights the velocity dispersion of the group and best-fit Gaussian and the core-dominated nature of the radio component of TXS 0206–048 in the inset panels at the top left and top right, respectively.

ORCID iDs

Sean D. Johnson  <https://orcid.org/0000-0001-9487-8583>
 Joop Schaye  <https://orcid.org/0000-0002-0668-5560>
 Gregory L. Walth  <https://orcid.org/0000-0002-6313-6808>
 Jennifer I-Hsiu Li  <https://orcid.org/0000-0002-0311-2812>
 Gwen C. Rudie  <https://orcid.org/0000-0002-8459-5413>
 Hsiao-Wen Chen  <https://orcid.org/0000-0001-8813-4182>
 Mandy C. Chen  <https://orcid.org/0000-0002-8739-3163>
 Massimo Gaspari  <https://orcid.org/0000-0003-2754-9258>
 Sebastiano Cantalupo  <https://orcid.org/0000-0001-5804-1428>
 Wolfram Kollatschny  <https://orcid.org/0000-0002-0417-1494>
 Zhuoqi (Will) Liu  <https://orcid.org/0000-0002-2662-9363>
 Sowgat Muzahid  <https://orcid.org/0000-0003-3938-8762>

References

- Abraham, R. G., Glazebrook, K., McCarthy, P. J., et al. 2004, *AJ*, 127, 2455
 Arav, N., Borguet, B., Chamberlain, C., Edmonds, D., & Danforth, C. 2013, *MNRAS*, 436, 3286
 Arnaud, M., Pratt, G. W., Piffaretti, R., et al. 2010, *A&A*, 517, A92
 Astropy Collaboration, Price-Whelan, A. M., Sipőcz, B. M., et al. 2018, *AJ*, 156, 123
 Bacon, R., Accardo, M., Adjali, L., et al. 2010, *Proc. SPIE*, 7735, 773508
 Bacon, R., Conseil, S., Mary, D., et al. 2017, *A&A*, 608, A1
 Balogh, M. L., Morris, S. L., Yee, H. K. C., Carlberg, R. G., & Ellingson, E. 1999, *ApJ*, 527, 54
 Becker, R. H., White, R. L., Gregg, M. D., et al. 2001, *ApJS*, 135, 227
 Bertin, E., & Arnouts, S. 1996, *A&AS*, 117, 393
 Bolton, A. S., Schlegel, D. J., Aubourg, E., et al. 2012, *AJ*, 144, 144
 Borisova, E., Cantalupo, S., Lilly, S. J., et al. 2016, *ApJ*, 831, 39
 Boselli, A., Epinat, B., Contini, T., et al. 2019, *A&A*, 631, A114
 Burchett, J. N., Rubin, K. H. R., Prochaska, J. X., et al. 2021, *ApJ*, 909, 151
 Butsky, I. S., Fielding, D. B., Hayward, C. C., et al. 2020, *ApJ*, 903, 77
 Cai, Z., Cantalupo, S., Prochaska, J. X., et al. 2019, *ApJS*, 245, 23
 Cantalupo, S., Arrigoni-Battaia, F., Prochaska, J. X., Hennawi, J. F., & Madau, P. 2014, *Natur*, 506, 63
 Cantalupo, S., Pezzulli, G., Lilly, S. J., et al. 2019, *MNRAS*, 483, 5188
 Chen, H. W., Boettcher, E., Johnson, S. D., et al. 2019, *ApJL*, 878, L33
 Chen, H. W., Gauthier, J. R., Sharon, K., et al. 2014, *MNRAS*, 438, 1435
 Chen, H. W., Zahedy, F. S., Johnson, S. D., et al. 2018, *MNRAS*, 479, 2547
 Chen, M. C., Chen, H. W., Rauch, M., et al. 2022, *MNRAS*, in press
 Chen, S. F. S., Simcoe, R. A., Torrey, P., et al. 2017, *ApJ*, 850, 188
 Chen, Y., Steidel, C. C., Erb, D. K., et al. 2021, *MNRAS*, 508, 19
 Coil, A. L., Weiner, B. J., Holz, D. E., et al. 2011, *ApJ*, 743, 46
 Correa, C. A., Schaye, J., Wyithe, J. S. B., et al. 2018, *MNRAS*, 473, 538
 Decarli, R., Dotti, M., Banados, E., et al. 2019, *ApJ*, 880, 157
 Dekel, A., Birnboim, Y., Engel, G., et al. 2009, *Natur*, 457, 451
 Epinat, B., Contini, T., Finley, H., et al. 2018, *A&A*, 609, A40
 Faber, S. M., Willmer, C. N. A., Wolf, C., et al. 2007, *ApJ*, 665, 265
 Faucher-Giguere, A. C. 2019, arXiv:1903.08657
 Ferland, G. J., Chatzikos, M., Guzmán, F., et al. 2017, *RMxAA*, 53, 385
 Finn, C. W., Morris, S. L., Crighton, N. H. M., et al. 2014, *MNRAS*, 440, 3317
 Finn, C. W., Morris, S. L., Tejos, N., et al. 2016, *MNRAS*, 460, 590
 Fossati, M., Fumagalli, M., Lofthouse, E. K., et al. 2021, *MNRAS*, 503, 3044
 Fu, H., Xue, R., Prochaska, J. X., et al. 2021, *ApJ*, 908, 188
 Fumagalli, M., Fossati, M., Hau, G. K. T., et al. 2014, *MNRAS*, 445, 4335
 Gaspari, M., Churazov, E., Nagai, D., Lau, E. T., & Zhuravleva, I. 2014, *A&A*, 569, A67
 Gaspari, M., Eckert, D., Ettori, S., et al. 2019, *ApJ*, 884, 169
 Gaspari, M., McDonald, M., Hamer, S. L., et al. 2018, *ApJ*, 854, 167
 Goulding, A. D., Greene, J. E., Bezanson, R., et al. 2018, *PASJ*, 70, S37
 Green, J. C., Froning, C. S., Osterman, S., et al. 2012, *ApJ*, 744, 60
 Greene, J. E., Zakamska, N. L., Ho, L. C., & Barth, A. J. 2011, *ApJ*, 732, 9
 Groves, B. A., Dopita, M. A., & Sutherland, R. S. 2004, *ApJS*, 153, 75
 Guo, H., Liu, X., Shen, Y., et al. 2019, *MNRAS*, 482, 3288
 Helton, J. M., Johnson, S. D., Greene, J. E., & Chen, H.-W. 2021, *MNRAS*, 505, 5497
 Herenz, E. C., Urrutia, T., Wisotzki, L., et al. 2017, *A&A*, 606, A12
 Hess, K. M., Cluver, M. E., Yahya, S., et al. 2017, *MNRAS*, 464, 957
 Hewett, P. C., & Wild, V. 2010, *MNRAS*, 405, 2302

- Ho, S. H., Martin, C. L., Kacprzak, G. G., & Churchill, C. W. 2017, *ApJ*, **835**, 267
- Hodges-Kluck, E. J., Miller, M. J., & Bregman, J. N. 2016, *ApJ*, **822**, 21
- Hoffmann, S. L., Mack, J., Avila, R., et al. 2021, AAS Meeting Abstracts, **53**, 216.02
- Johnson, S. D., Chen, H.-W., & Mulchaey, J. S. 2013, *MNRAS*, **434**, 1765
- Johnson, S. D., Chen, H. W., Straka, L. A., et al. 2018, *ApJL*, **869**, L1
- Johnson, S. D., Mulchaey, J. S., Chen, H.-W., et al. 2019, *ApJL*, **884**, L31
- Kennicutt, R. C., & Evans, N. J. 2012, *ARA&A*, **50**, 531
- Konidaris, N. P., Rudie, G. C., Newman, A. B., et al. 2020, *Proc. SPIE*, **11447**, 114471E
- Krug, H. B., Rupke, D. S. N., & Veilleux, S. 2010, *ApJ*, **708**, 1145
- Lacy, M., Baum, S. A., Chandler, C. J., et al. 2020, *PASP*, **132**, 035001
- Leclercq, F., Verhamme, A., Epinat, B., et al. 2022, arXiv:2203.05614
- Lehner, N., & Howk, J. C. 2011, *Sci*, **334**, 955
- Leitner, S. N., & Kravtsov, A. V. 2011, *ApJ*, **734**, 48
- Li, Y., Gendron-Marsolais, M.L., Zhuravleva, I., et al. 2020, *ApJL*, **889**, L1
- Liu, G., Zakamska, N. L., Greene, J. E., Nesvadba, N. P. H., & Liu, X. 2013, *MNRAS*, **430**, 2327
- Lopez, S., Tejos, N., Ledoux, C., et al. 2018, arXiv 1801.10175
- Mandelker, N., van?den?Bosch, F. C., Nagai, D., et al. 2020, *MNRAS*, **498**, 2415
- Martin, C., Moore, A., Morrissey, P., et al. 2010, *Proc. SPIE*, **7735**, 77350M
- Martin, C. L., Shapley, A. E., Coil, A. L., et al. 2012, *ApJ*, **760**, 127
- McDonald, M., Bayliss, M., Benson, B. A., et al. 2012, *Natur*, **488**, 349
- McDonald, M., Veilleux, S., Rupke, D. S. N., & Mushotzky, R. 2010, *ApJ*, **721**, 1262
- Moreno, J., Torrey, P., Ellison, S. L., et al. 2021, *MNRAS*, **503**, 3113
- Munari, E., Biviano, A., Borgani, S., Murante, G., & Fabjan, D. 2013, *MNRAS*, **430**, 2638
- Nelson, D., Sharma, P., Pillepich, A., et al. 2020, *MNRAS*, **498**, 2391
- Nesvadba, N. P. H., Drouart, G., De Breuck, C., et al. 2017, *A&A*, **600**, A121
- O'Sullivan, D. B., Martin, C., Matuszewski, M., et al. 2020, *ApJ*, **894**, 3
- Oppenheimer, B. D., Segers, M., Schaye, J., Richings, A. J., & Crain, R. A. 2018, *MNRAS*, **474**, 4740
- Piqueras, L., Conseil, S., Shepherd, M., et al. 2017, arXiv 1710.03554
- Poggianti, B. M., Jaffe, Y. L., Moretti, A., et al. 2017, *Natur*, **548**, 304
- Punsly, B., Marziani, P., Zhang, S., Muzahid, S., & Dea, C. P. 2016, *ApJ*, **830**, 104
- Putman, M. E. 2017, in Gas Accretion onto Galaxies, ed. A. Fox & R. Davé, Vol. 430 (Berlin: Springer), 1
- Putman, M. E., Peek, J. E. G., & Joung, M. R. 2012, *ARA&A*, **50**, 491
- Qu, Z., Chen, H. W., Rudie, G. C., et al. 2022, *MNRAS*, **516**, 4882
- Rauch, M., Becker, G. D., Haehnelt, M. G., et al. 2011, *MNRAS*, **418**, 1115
- Rauch, M., Becker, G. D., & Haehnelt, M. G. 2016, *MNRAS*, **455**, 3991
- Richards, G. T., Lacy, M., Storrie-Lombardi, L. J., et al. 2006, *ApJS*, **166**, 470
- Robitaille, T., & Bressert, E. 2012, APLpy: Astronomical Plotting Library in Python, Astrophysics Source Code Library, ascl:1208.017
- Rubin, K. H. R. 2017, in Gas Accretion onto Galaxies, ed. A. Fox & R. Davé, Vol. 430 (Berlin: Springer), 95
- Rubin, K. H. R., Prochaska, J. X., Koo, D. C., & Phillips, A. C. 2012, *ApJL*, **747**, L26
- Rupke, D. S. N., Coil, A., Geach, J. E., et al. 2019, *Natur*, **574**, 643
- Sato, T., Martin, C. L., Noeske, K. G., Koo, D. C., & Lotz, J. M. 2009, *ApJ*, **696**, 214
- Shen, Y., Richards, G. T., Strauss, M. A., et al. 2011, *ApJS*, **194**, 45
- Smolcic, V., Intema, H., Slaus, B., et al. 2018, *A&A*, **620**, A14
- Soto, K. T., Lilly, S. J., Bacon, R., Richard, J., & Conseil, S. 2016, ZAP: Zurich Atmosphere Purge, Astrophysics Source Code Library, ascl:1602.003
- Stern, J., Faucher-Giguere, C.-A., Zakamska, N. L., & Hennawi, J. F. 2016, *ApJ*, **819**, 130
- Tacconi, L. J., Neri, R., Genzel, R., et al. 2013, *ApJ*, **768**, 74
- Tejos, N., Morris, S. L., Finn, C. W., et al. 2014, *MNRAS*, **437**, 2017
- Thatte, N., Tecza, M., Schnetler, H., et al. 2021, *Msng*, **182**, 7
- Tumlinson, J., Peebles, M. S., & Werk, J. K. 2017, *ARA&A*, **55**, 389
- van de Voort, F., & Schaye, J. 2012, *MNRAS*, **423**, 2991
- Vanzella, E., Balestra, I., Gronke, M., et al. 2017, *MNRAS*, **465**, 3803
- Weilbacher, P. M., Palsa, R., Streicher, O., et al. 2020, *A&A*, **641**, A28
- Weilbacher, P. M., Streicher, O., Urrutia, T., et al. 2014, in ASP Conf. Ser. 485, Astronomical Data Analysis Software and Systems XXIII, ed. N. Manset & P. Forshay (San Francisco, CA: ASP), 451
- Weiner, B. J., Coil, A. L., Prochaska, J. X., et al. 2009, *ApJ*, **692**, 187
- Werk, J. K., Prochaska, J. X., Tumlinson, J., et al. 2014, *ApJ*, **792**, 8
- Zabl, J., Bouche, N. F., Schroetter, I., et al. 2019, *MNRAS*, **485**, 1961
- Zabl, J., Bouche, N. F., Wisotzki, L., et al. 2021, *MNRAS*, **507**, 4294
- Zahedy, F. S., Chen, H. W., Johnson, S. D., et al. 2019, *MNRAS*, **484**, 2257
- Zakamska, N. L., Strauss, M. A., Krolík, J. H., et al. 2006, *AJ*, **132**, 1496